

Article

# A Design for Vortex Suppression Downstream of a Submerged Gate

Ender Demirel <sup>1,\*</sup>  and Mustafa M. Aral <sup>2</sup>

<sup>1</sup> Department of Civil Engineering, Eskisehir Osmangazi University, Eskisehir 26480, Turkey

<sup>2</sup> Design and Simulation Technologies Inc., DSTECH, Eskisehir 26480, Turkey; mmara1@dstechno.net

\* Correspondence: edemirel@ogu.edu.tr; Tel.: +90-222-2393750

Received: 10 January 2020; Accepted: 6 March 2020; Published: 9 March 2020



**Abstract:** Interaction of recirculating and mean flow downstream of a submerged gate may form significant vortex structures, which may affect the stability of the gate. Although these flow structures that appear in submerged hydraulic jumps received considerable attention in the literature, relatively less work was devoted to the analysis and suppression of the vortex structures downstream of a submerged gate. In this work, internal flow structure and vortex dynamics around a submerged gate were investigated through laboratory tests and large-eddy simulation (LES) using computational fluid dynamics (CFD). It is shown that numerical results obtained for mean velocity field are in good agreement with the experimental measurements. A helical vortex pair connected with a horseshoe vortex system was identified within the roller region using high-resolution numerical simulations. Damping performance of different types of anti-vortex elements placed on the downstream face of the gate are evaluated based on numerical studies. It is shown that the horizontal porous baffle mounted at an elevation below the free surface reduced the vortex magnitudes in the roller region by 26.8%. With the implementation of the proposed vortex breaker, lift forces acting on the gate lip were reduced by 9.4% and drag forces acting on the downstream face of the gate were reduced by 8.6%. Finally, in this study, we assess the performance of the vortex breaker under different flow conditions.

**Keywords:** vertical gate; submerged jump; large eddy simulation; anti-vortex element

## 1. Introduction

Vertical gates were used in the past decade to regularize seasonal variations in streams under a broad range of operational conditions. A submerged hydraulic jump (SHJ) occurs downstream of the gate when the tail water depth exceeds the conjugate subcritical depth of the free jump and a reverse flow occurs above the wall jet. Typically, upstream flow that passes below the gate strongly interacts with the reverse flow (Figure 1) in the roller region, and this interaction creates spatially and temporally varying vortex structures around the gate. Vortex-induced hydrodynamic effects acting on the gate may lead to the oscillation and breakdown of the gate structure depending on flow conditions. Thus, a clear understanding of the three-dimensional features of the vortex structure around the gate is necessary to develop novel designs that would reduce the hydrodynamic effects that act on the gate, which is the main aim of the present study.

A large number of experimental studies were carried out to investigate the flow features in the SHJ. Long et al. [1] examined the turbulent flow structure of the SHJ in terms of surface profiles, mean velocity components, and Reynolds stresses for various Froude numbers and submergence ratios. Vertical distribution of the velocity measurements at different spanwise locations revealed that the flow structure in the SHJ is three-dimensional due to vortex motions near the gate. Demirel [2] conducted series of experimental studies for the investigation of SHJ under different flow conditions and concluded that the interaction of mean and reverse flows caused the formation of two corner

vortices downstream of the gate. Vortex induced free-surface fluctuations observed in the vicinity of the structure were found to play an important role in creating hydrodynamic forces on the gate. Liu et al. [3] experimentally investigated the turbulence structure of the hydraulic jump at low Froude numbers and the dominant frequency was found to be in the range 0 to 4 Hz for both horizontal and vertical velocity components. Dynamics of vortices in the SHJ were experimentally investigated by Dios et al. [4] using acoustic doppler velocimetry (ADV) and particle tracking velocimetry (PTV) in terms of mean flow and turbulence statistics at different vertical planes. The relationship between the length scales of the roller and the vortices revealed the strong coherent motion of vortex structure in the SHJ. Characteristics of the submerged wall jet on the rough bed were extensively investigated, and it was shown that the rate of jet decay in submerged jump increased with increase in bed roughness [5,6]. Although experimental studies emphasized the strong motion of vortices near the gate, the three-dimensional features of the vortex field around the gate remain to be thoroughly investigated due to the inherent limitations of experimental measurements.

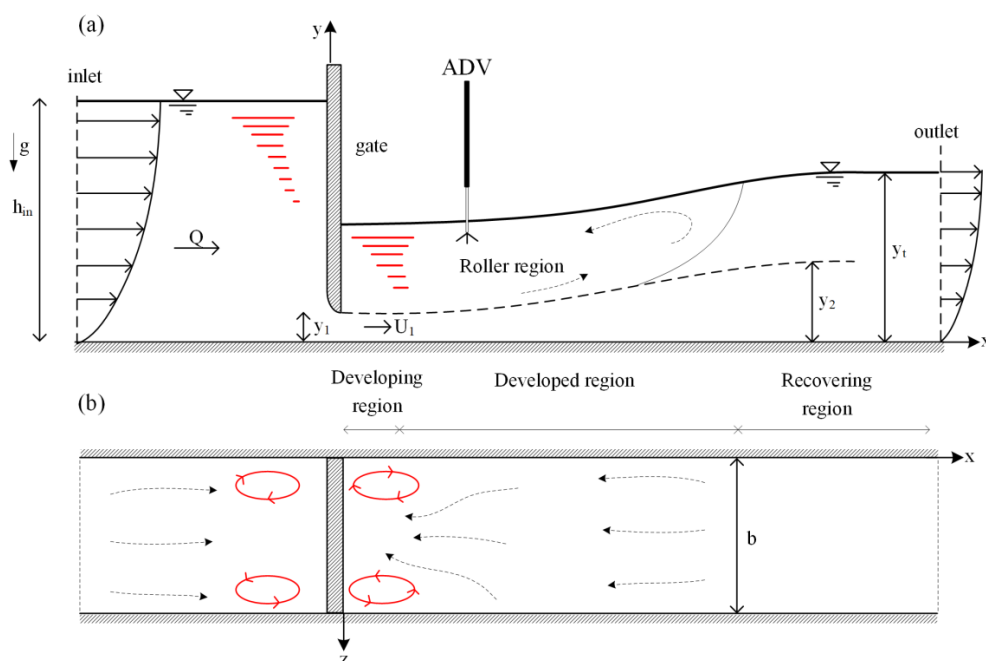


**Figure 1.** Sketch of the turbulent flow through a submerged vertical gate: (a) lateral view; (b) top view.

The flow around the gate is three-dimensional and unsteady due to the interaction of the vortices with the mean flow, which produces counter-rotating vortices at the upstream and forms a roller region at the downstream of the gate (Figure 1). The reverse flow in the roller region interacts with the vortex-induced flow and creates two counter-rotating vortices downstream of the gate (Figure 1b). Several researchers conducted experimental studies in an attempt to evaluate the vortex-induced hydrodynamic pressures acting on the gate. Bhargava et al. [7] conducted experimental studies in a laboratory flume to investigate the hydrodynamic pressures on the gate lip in terms of mean and fluctuating pressure coefficients. Thang and Naudascher [8] studied the vortex-excited vibration of underflow lift gates experimentally. They observed that the dynamic interaction between the gate and unstable shear layer may produce periodic vortex shedding that oscillates the gate. Turbulent flow-induced multiple mode vibration of the submerged gate was experimentally investigated by Billeter and Staubli [9] based on simultaneous measurements of velocity and pressure. Transition to galloping flow structure was found to play a significant role in the production of instability-induced excitation for the reduced velocities ranging from 0.8 to 14 (dimensionless). Cross-flow vibrations of underflow gates were experimentally investigated by Erdbrink et al. [10] using resistance-type water level and force meter equipment. Studies identified that the vortex flow around the submerged gate

may play a critical role in the onset of vibration of the structure due to hydrodynamic effects. The present study focuses on the formation of vortices around the submerged gate and the hydrodynamic forces acting on the structure, which are critical issues for the design of vortex damping structures that may eliminate damage to gate structures.

Numerical simulations of complex flows around submerged structures made it possible to evaluate the internal flow features of turbulent flows. Two-dimensional Reynolds-averaged Navier–Stokes (RANS)-based numerical models were first attempted in the literature to simulate turbulent flows in the SHJ [11–14]. While these studies provided insights into the turbulence structure of low- and high-Froude-number flows, the two-dimensional numerical models could not predict the formation of vortex structure around the submerged gate. An assessment of the literature on the numerical simulation of the SHJ clearly shows that the RANS-based numerical models may suffer from inaccurate simulation of vortex structures that form both at the upstream and at the downstream of the gate due to strong coherent motions and energetic eddies. Eddy resolving computational models are alternatively used to simulate unsteady dynamics of coherent structures that are present near the gate. In order to overcome this limitation of RANS-based numerical models, Jesudhas et al. [15] performed a detached eddy simulation (DES) of the SHJ with an incident Froude number of 8.2 to examine the coherent structure of the three-dimensional turbulent flow field in the developing and developed zones. The limitation of this numerical study is that they focused on the flow downstream of the gate while imposing an inlet velocity field below the gate and the flow upstream of the gate was not simulated, which may play an important role in the formation of vortex structures around the gate. A large number of numerical studies were conducted in the literature to understand the flow features downstream of the gate, but the three-dimensional features of the vortex formation around the submerged gate were not reported.

The present experimental and numerical study considers turbulent flow underneath the submerged vertical gate in a flat-bed channel as schematically shown in Figure 1. Constant flow rate  $Q$  enters the channel at the inlet and emerges from the outlet of the domain to maintain constant water depths of  $h_{in}$  and  $y_t$  at the upstream and downstream of the channel, respectively. The Froude number of the flow is defined based on the gate opening  $y_1$  and average flow velocity  $U_1$  below the gate as  $F_1 = U_1 / \sqrt{gy_1}$ , where  $g$  is the gravitational acceleration. The corresponding Reynolds number of the flow is defined based on the hydraulic radius ( $R$ ) below the gate as  $R = 4U_1R/v$ , where  $v$  is the kinematic viscosity. Here for submerged flow conditions, the tail water depth  $y_t$  is greater than the water depth  $y_2$ , which is the subcritical conjugate depth of the  $y_1$  as obtained from the Belanger equation. The corresponding submergence factor can be calculated as  $S = (y_t - y_2) / y_2$ .

The aim of this study is to gain a deeper understanding of flow and turbulence structures, as well as vortex generation around a submerged gate using experimental and numerical analysis, with the goal of developing vortex damping structures downstream of the gate. Experimental studies were conducted in a laboratory flume to evaluate and validate the numerical model. Time-averaged flow velocities and turbulence stresses were measured using ADV at different locations downstream of the gate. Recognizing that the coherent motions of vortices may result in hydrodynamic effects on the gate, LES studies were performed to analyze hydrodynamic effects acting on the submerged vertical gate for different inlet Froude numbers and submergence ratios. The first objective of the present study is to reveal the three-dimensional flow structure and vortex formations at both upstream and downstream of the gate. Achievement of this goal will allow us to understand the connection between upstream and downstream flows since the incident vortex flow strongly interacts with the recirculating flow downstream of the gate. The second objective is to analyze vortex-induced hydrodynamic forces acting the submerged gate using high-resolution numerical simulations. The third objective is to develop a vortex breaker to mitigate the adverse hydrodynamic effects acting on the gate. Performance of the proposed vortex breaker was evaluated for different flow conditions in terms of mean and instantaneous flow fields, as well as hydrodynamic forces acting on the gate body.

## 2. Flume Experiments

Experimental studies were conducted in a laboratory flume, which was 10 m long, 40 cm wide, and 60 cm high with plexiglass sidewalls and a stainless-steel bottom. Water was supplied from a large water tank using a pump with 100 L/s maximum flow rate capacity. Flow discharge at the inlet of the flume was controlled by a valve manually and measured using the ultrasonic flow meter mounted on the feeding pipe. Supercritical depth was produced using a vertical gate located at the upstream of the flume, and the tail water depth was provided using a tilting gate located at the downstream end of the flume to adjust for the desirable incident Froude number and submergence factor, which are the key parameters to characterize the flow through the submerged gate.

A downward-looking 200-Hz Nortek ADV was used to measure velocity components instantaneously at a cylindrical sampling volume of 5 cm below the ADV probe. Velocity components were spatially averaged in the sampling volume to collect enough data near the sampling point. The use of a relatively larger sampling volume in the near bed region may cause unrealistic velocity measurements since the sampling volume may not be representative of the main flow region. Thus, a smaller sampling volume was used near the channel bed to satisfy the signal-to-noise ratio (SNR) being greater than 20, which is recommended by the manufacturer of the ADV [16]. Other critical parameters of the ADV measurements were nominal velocity range (NVR), transmit length (TL), and power level (PL), to adjust the range of flow velocities, the length of the transmitted wave from the ADV probe, and the power level of the electricity to be generated by the ADV, respectively. Details of the experimental set-up can be found in Demirel [2]. Optimum parameters of the ADV were adjusted such that the  $SNR > 20$  in both near-wall and roller regions. ADV measurements were conducted in the laboratory for the flow conditions given in Table 1.

**Table 1.** Flow characteristics of the experimental study.

Q (L/s)	$y_1$ (mm)	U1 (m/s)	$F_1$	R	$y_2$ (mm)	$y_t$ (mm)	S
21	25	2.1	4.24	98,824	137.93	230	0.67

The flow in the flume was recirculated about 2 h with a constant flow rate before the velocity measurements commenced to exclude initial conditions, as well as to satisfy mass conservation in the roller region. Velocity at a point was measured for 180 s in order to collect adequate data and to obtain time-averaged flow quantities. Velocity data may contain spikes due to noise effects with the reflection of transmitted acoustic waves near the bed. In this study, the raw data were filtered using WinADV software [17]. A snapshot of the experimental study is given in Figure 2. The ADV was attached to a mobile traverse table in order to fix the ADV probes to a specific measurement point.

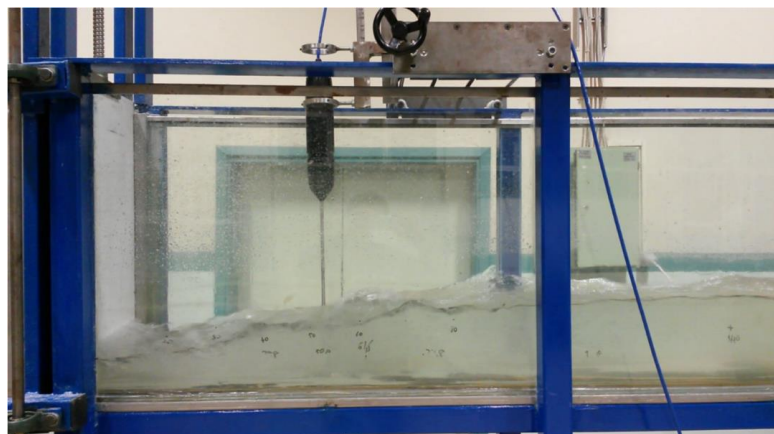


**Figure 2.** Snapshot of the experimental set-up. A supplementary video file is available for the animation of the experimental study.

ADV measurements were conducted at different spanwise locations in order to determine at which stations the three-dimensional effects were significant. Vertical distributions of time-averaged streamwise velocity component at  $x/y_1 = 5$  are depicted for different spanwise locations in Figure 3a. Dimensionless jet velocity below the gate is about 1.2 and almost independent of the backward effects since the flow with high momentum is strongly in the downstream direction in this region. However, recirculation effects tend to increase near the free surface due to the fact that the baroclinic torque caused by the high gradient of fluid density along the air–water interface generates vortex motion [18]. As seen in Figure 3b, the maximum spanwise velocity is observed at  $z/b = 0.4$ , at which station the vorticity effects are expected to be considerable. While normalized Reynolds stresses in horizontal ( $\sqrt{u'^2}/U_1$ ) and vertical ( $\sqrt{v'^2}/U_1$ ) directions seem to be identical, the vertical distributions of Reynolds stress in the spanwise direction ( $\sqrt{w'^2}/U_1$ ) are variable, and the maximum value is observed at  $z/b = 0.4$ , which is consistent with the previous observations in the literature [1]. While the normal components of Reynolds stresses in horizontal and vertical directions are identical at each measurement station, the spanwise component of Reynolds stress exhibits a significant variation due to the energetic vortex structures observed on the free surface.

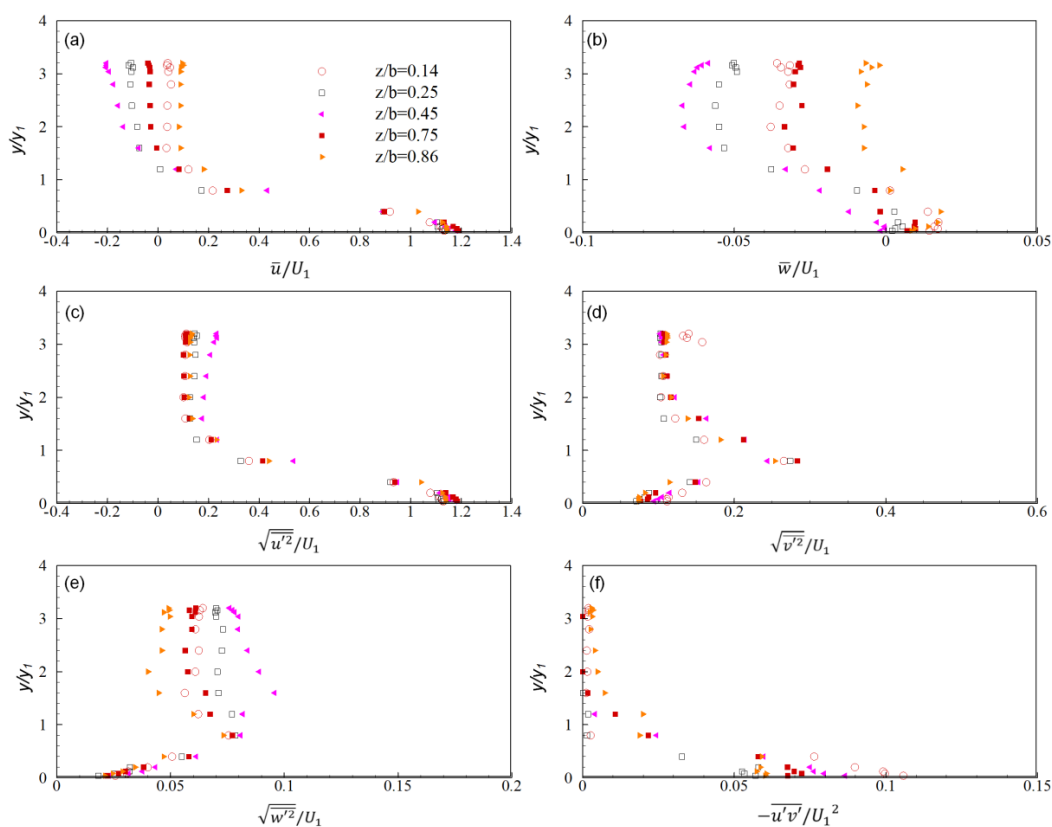


**Figure 3.** Vertical distributions of dimensionless mean velocity components and Reynolds stresses at  $x/y_1 = 5$ . Velocity components are compared in (a,b); Reynolds stresses are compared in (c–f).

### 3. Computational Model

#### 3.1. Numerical Framework

LES is employed in the present study in order to capture dynamics of coherent flow structures around the gate. The unsteady, incompressible and turbulent flow is simulated based on spatially filtered Navier–Stokes equations in the LES approach.

$$\frac{\partial \tilde{u}_i}{\partial x_i} = 0, \quad (1)$$

$$\frac{\partial \tilde{u}_i}{\partial t} + \frac{\partial \tilde{u}_i \tilde{u}_j}{\partial x_j} = -\frac{1}{\rho} \frac{\partial \tilde{p}}{\partial x_i} + \frac{\partial}{\partial x_j} \left[ v \left( \frac{\partial \tilde{u}_i}{\partial x_j} + \frac{\partial \tilde{u}_j}{\partial x_i} \right) \right] - \frac{\partial \tau_{ij}}{\partial x_j} + g_i + f_{\sigma i}, \quad (2)$$

where  $\tilde{u}_i$  and  $\tilde{p}$  are the filtered velocity components in the  $i$ -direction ( $x$ -,  $y$ -, and  $z$ -direction) and the hydrodynamic pressure, respectively,  $\rho$  is the density,  $t$  is the time,  $v$  is the kinematic viscosity,  $x_i$  and  $x_j$  represent the Cartesian coordinates,  $g_i$  is the gravitational acceleration in the  $i$ -direction, and  $f_{\sigma i}$  represents the surface tension, which is modeled as continuum surface force depending on the corresponding curvature of the free surface [19]. A Smagorinsky sub-grid scale (SGS) model is used for the evaluation of the unresolved subgrid-scale fluctuations of turbulent stresses  $\tau_{ij}$ . In the present LES implementation, subgrid-scale eddy viscosity is calculated based on the filter size  $(\Delta x \cdot \Delta y \cdot \Delta z)^3$  and the Smagorinsky constant  $C_s$ , which is fixed at 0.1 in the whole computational domain.

The volume of fluid (VOF) method by Hirt and Nichols [20] is used to track the nonlinear free-surface waves on the Eulerian mesh. The following advection equation is solved for the volume of fluid function  $F$ , which is introduced to represent the volume fraction of the fluid within a computational cell:

$$\frac{\partial F}{\partial t} + \frac{\partial u_i F}{\partial x_i} = 0. \quad (3)$$

Computational cells are tagged as water, air, and free-surface cells with respect to the  $F$  value at each time step of the simulation. In this study, numerical solutions of the governing equations are performed employing the solver interFOAM, which is available for the simulation of multiphase flows in open source code OpenFOAM [19]. The second-order Crank–Nicolson implicit method is used for the discretization of unsteady terms and the second-order linear method is used for the convective terms. Gradient terms in the governing equations are discretized using the second-order Gauss linear method. Thus, the overall numerical scheme used in the present study is second-order accurate in space and time, which yields accurate results for the prediction of spatial and temporal variations in vorticity. Iterations for the solution of the governing equations between two successive time steps were terminated when the residual terms of the momentum and turbulence equations were less than  $10^{-6}$ . The computational time step size was calculated according to the Courant stability condition during numerical simulations. The Courant number was set to  $Cr = 0.5$  for the momentum and advection equations in order to reduce truncation errors arising from the discretization of unsteady terms, even though the present solver may yield accurate results for the Courant number up to 6. As discussed in the subsequent part of the study, the Courant number was reduced to 0.3 in order to overcome stability problems arising from the simulation of flows around the vortex breakers, since such local changes applied on the gate required smaller time-step sizes during simulations. Time averaging was started from 120 s of the simulation in order to exclude unphysical unsteady effects arising from the initial conditions, and it was performed for 280 s, which is significantly larger than the time scales in the computational domain.

#### 3.2. Mesh and Boundary Conditions

The computational mesh should be fine enough to capture spatial and temporal variations of vortices in the roller region. A structured mesh was generated in the computational domain with grid

clustering near the walls and free surface to capture large gradients in the vicinity of the boundaries. The position of the free surface was first approximated using preliminary results of the numerical simulations on a relatively coarse mesh, and then the mesh was clustered near the free-surface. The length of the roller region  $L_{rsj}$  was estimated from the following empirical equation proposed by Wu and Rajaratnam [21], and the grid was refined in the roller region as shown in Figure 4b:

$$\frac{L_{rsj}}{y_2} = 6 + 4.14S. \quad (4)$$

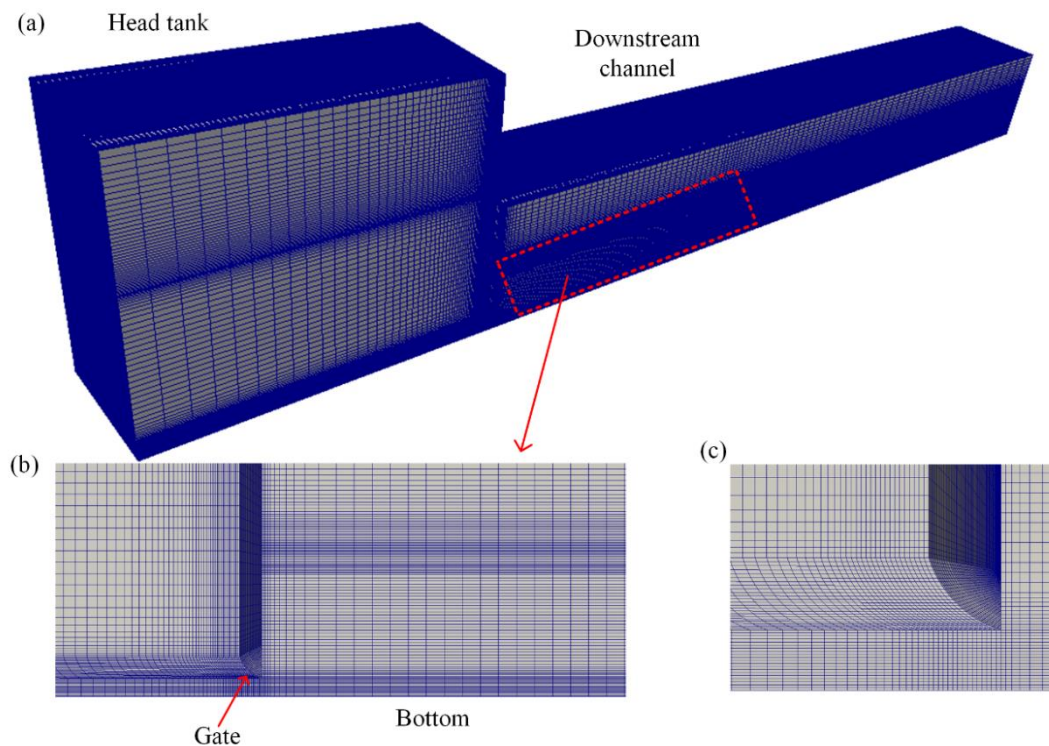


**Figure 4.** Block-structured computational mesh: (a) three-dimensional view of the mesh in the computational domain; (b) front view of the mesh in the roller region; (c) zoomed-in view of the gate lip.

A non-orthogonal mesh was used near the gate lip (Figure 4c) in order to capture curvilinear geometry in the present structured mesh system. Maximum non-orthogonality of the present mesh was  $71.5^\circ$ , which was acceptable for the simulation of the present problem. However, a non-orthogonal correction method with five steps was applied in order to increase the accuracy of the numerical solution in this region. Under these conditions the mesh was generated as seen in Figure 4a, and the flow was simulated yielding vortex flow at the entrance of the roller region. Most numerical studies in the literature used inlet boundary at a vertical section below the gate without solving upstream flow, and longitudinal inlet velocity distribution was imposed at the inlet [11]. This type of boundary condition cannot realistically mimic the flow conditions below the gate since the incident vortex flow below the gate may significantly affect the accuracy of the numerical simulations. Therefore, proper boundary conditions are required for velocity and free surface to maintain a constant water level at the upstream of the gate for a given flow rate. Free-surface level at the inlet is generally fixed using a Dirichlet-type boundary condition for a known water depth instead of coupling velocity field and free-surface level at the inlet. This approach requires the specification of an upstream water depth and has some drawbacks such as producing back flow near the free-surface and unrealistic free-surface profiles. Simulating turbulent flow in a long inlet channel would be another alternative way of obtaining a fully developed flow upstream of the gate. However, this type of simulation would

increase the computational time and the required memory to solve for the flow variables. In this study, an inlet boundary condition was incorporated into the solver to couple velocity field and free-surface height dynamically considering the following fully developed velocity profile at the inlet [14]:

$$u(y) = (\gamma + 1)U_0\left(\frac{y}{h_0}\right)^\gamma, \quad (5)$$

where  $\gamma$  is the shape factor, which is set to 0.1 for open channel flows,  $u$  is the horizontal velocity component, and  $U_0$  is the average flow velocity at the inlet, which is calculated by the solver as the ratio of the flow rate to the wetted area at the inlet section during the simulation. The wetted area is calculated at each time step as the summation of surface areas of the cells containing water  $\sum_{j=1}^{jmax} \sum_{k=1}^{kmax} F_{jk}(\Delta y_j \Delta z_k)$ , where  $\Delta y_j$  and  $\Delta z_k$  are cell sizes in  $y$ - and  $z$ -directions, respectively,  $jmax$  and  $kmax$  are the number of cells in  $y$ - and  $z$ -directions at the inlet section, and  $F_{jk}$  represents the volume fraction at the cell  $(j,k)$ . Thus, the inlet depth is not required to be specified in the pre-processing step, which provides us an algorithm to simulate flow problems in which inlet height is not known. The outlet boundary condition named “outletPhaseMeanVelocity” is used to adjust tail water depth according to the average flow velocity at the outlet of the channel.

In the numerical simulations, upstream and downstream channels are firstly filled up to 10 cm with water; then, the water depth at the inlet increases as the numerical simulation continues and stabilizes at a constant head when the mass conservation is satisfied in the entire computational domain. Turbulence intensity was set to 5% at the inlet, which is common for the simulation of open channel flows, and turbulence kinetic energy was calculated according to the specified turbulence intensity using the equation  $k = 1.5(UI)^2$ , where  $U$  is the mean flow velocity and  $I$  is the turbulence intensity. A no-slip boundary condition was imposed for the velocity, and unified wall functions were used for the turbulence on the walls. Although a steady-state flow field was imposed below the gate without simulating the flow upstream of the gate in previous numerical studies, the simulation of the upstream flow in this study provided a fluctuating flow field below the gate, which is critical for the investigation of vortex structures downstream of the gate. As the turbulent flow develops at the upstream channel and impinges on the gate due to the stagnation of the upstream flow, the required turbulent flow conditions free of upstream boundary conditions are maintained below the gate. The upstream boundary is far away from the gate region and its effects are dissipated along the distance from the inlet to the gate opening. The upstream flow impinges on the gate and a vortex pair forms, which has more influence on the flow structure under the gate. Thus, the structure of the turbulent flow emerging from the gate opening is not sensitive to the turbulence boundary conditions applied at the inlet of the upstream channel. However, moving the upstream boundary far away from the gate area is necessary to provide the necessary degree of freedom to the region underneath the gate for the flow structure to establish itself in that region free of boundary effects. This necessary condition was implemented in this application. The time-step size took the values of  $\Delta t \approx 10^{-4}$  s for the present computational mesh during the simulation. The computational domain was decomposed to 112 subdomains, and the numerical simulations were performed on the High-Performance and Grid Computing Center (TRUBA) [22] using 112 computational nodes on Linux machines (Intel E-5 2690 v4 2.60GHz) to obtain accurate results with high resolution. The wall time of each case was about 50 h depending on the Froude number since the time-step size reduces as the flow velocity increases according to the stability condition for unsteady flow simulations.

## 4. Results and Discussion

### 4.1. Mesh Independent Study and Validation

Vertical distributions of the simulated mean streamwise velocity component at  $x/y_1^+ = 5$  and  $z/b = 0.45$  were compared with the experimental measurements using different grids in order to assess the resolution of the computational mesh. Properties of the grids used in the mesh independent study are given in Table 2 along with the dimensionless wall distance as minimum, average, and maximum values over the bottom of the channel. The calculated wall distances over the remaining walls are not shown here. The average value of the  $y^+$  stabilized for Mesh 3 since the variation of  $y^+$  was negligible in Mesh 4.

**Table 2.** Grid parameters used in mesh independent study.

Grid	Number of Cells ( $\times 10^6$ )	$(y^+)_{min}$	$(y^+)_{average}$	$(y^+)_{max}$	$(x^+)_{min}$	$(x^+)_{average}$	$(x^+)_{max}$
Mesh 1	0.7	2.20	53.05	176.09	0.25	23.10	83.36
Mesh 2	1.85	0.84	26.95	91.86	0.22	13.42	45.65
Mesh 3	2.60	0.93	27.38	90.09	0.14	12.82	41.50
Mesh 4	4.10	1.15	28.16	94.74	0.04	9.86	35.42

The present mesh consists of about 4.1 million computational cells, and the time-step size takes the values of  $\Delta t = 10^{-4}$  s during the simulation according to the stability criteria. Figure 5 shows that the three-dimensional effects are prominent at  $z/b = 0.4$  since recirculation effects produce negative velocity magnitudes near the free surface. Thus, velocity profiles in the streamwise direction were measured  $z/b = 0.4$  and compared with the present numerical results in Figure 6a to validate the present computational model for severe conditions. The present numerical model can accurately predict the streamwise variation of mean velocity. The near-wall profile of the horizontal velocity component is depicted in Figure 6b. A linear velocity distribution is obtained near the wall due to the wall functions used in the numerical simulations.

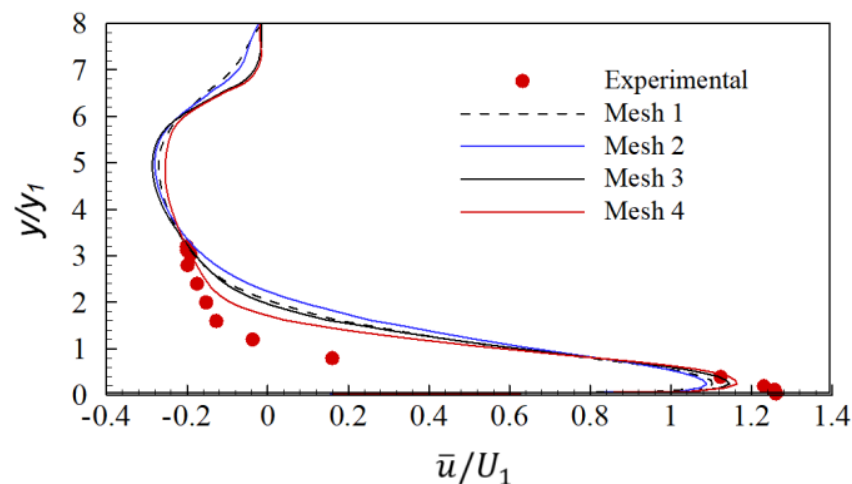


**Figure 5.** Comparison of velocity profiles at  $x/y_1 = 5$  and  $z/b = 0.4$  for different mesh resolutions.

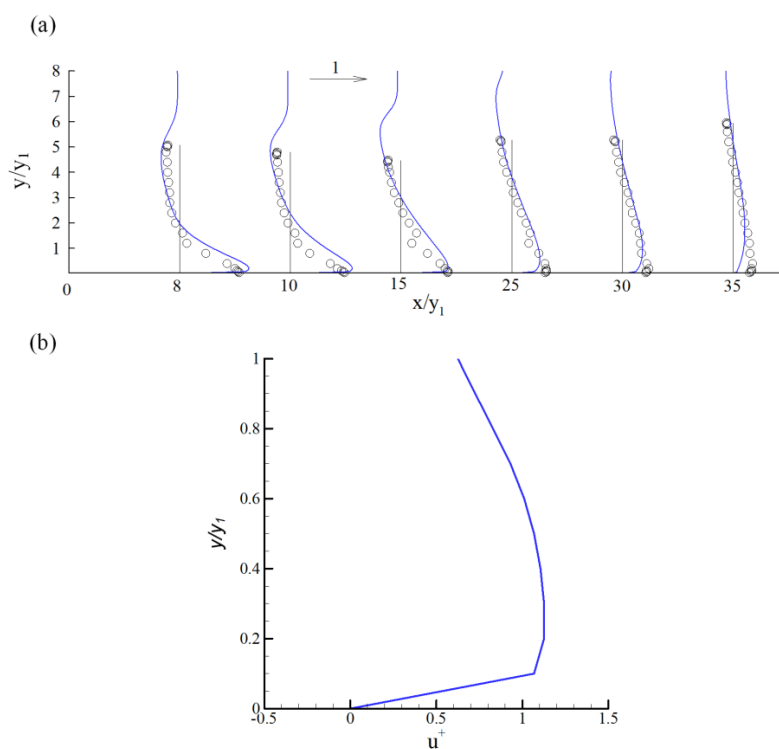
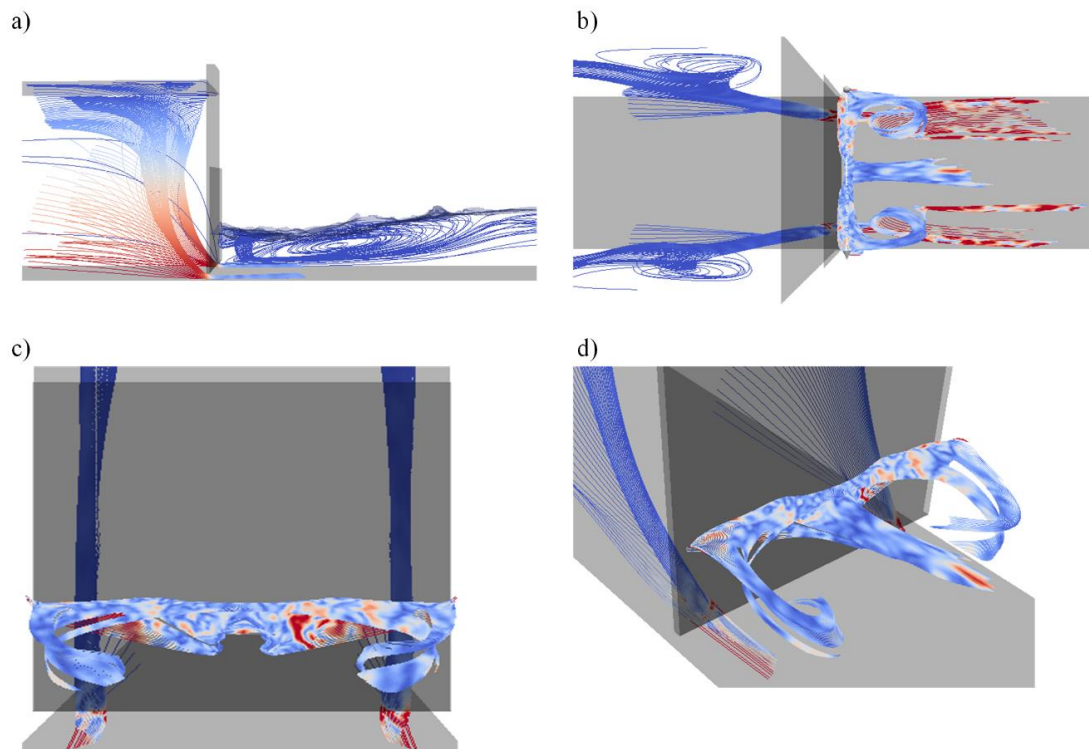


**Figure 6.** (a) Comparison of vertical distributions of dimensionless time-averaged horizontal velocity components at  $z/b = 0.4$ . The solid line represents numerical results and symbols represent experimental measurements. (b) Near-wall profile of time-averaged horizontal velocity component.

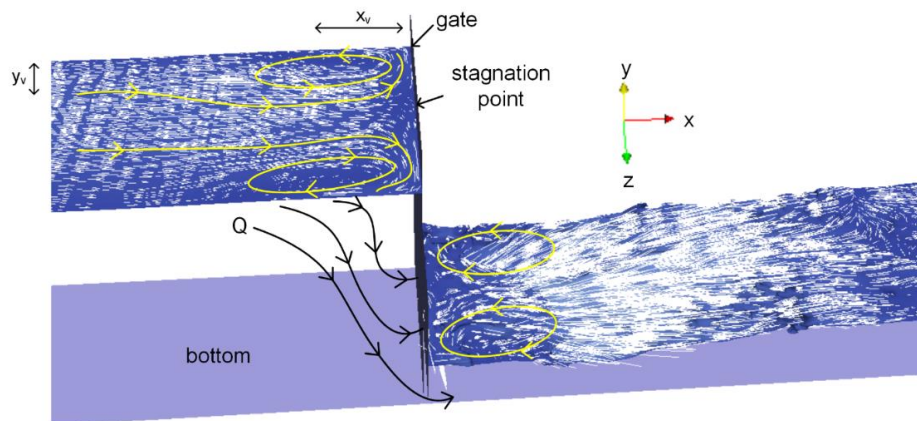
#### 4.2. Mean Flow Structure around the Gate

Figure 7 shows the three-dimensional view of time-averaged streamlines and free-surface patterns at the upstream and downstream channels. As the flow approaches the gate, the flow splits into two parts and creates two counter-rotating vortices near the corners. As seen in Figure 8, locations of the vortex cores relative to the gate and sidewall are determined as  $x_v \approx 0.12 \text{ m}$  and  $y_v \approx 0.04 \text{ m}$ , respectively. Similar corner vortices corresponding to the stagnation flow upstream from the gate were observed experimentally by Roth and Hager [23]. Significant vorticity effects are observed on the free surface since the baroclinic torque caused by the dynamic pressure gradient along the air–water interface creates vortices near the regions where density difference is high [18]. Upstream vortices strongly connect to the downstream flow to create a complex flow field in the roller region. The length of the roller region was estimated as  $L_{rsj} = 0.92 \text{ m}$  from the numerical simulation results. Numerical results show that the present computational model can simulate vorticity generation mechanism near the gate.

Recirculating flow that forms above the submerged plane jet splits into two parts and vortex pair forms associated with the impingement of the recirculating flow on the downstream face of the gate. Counter-rotating vortices observed downstream of the gate stretch downward at depth as tornado-like vortices, which subsequently connect to the submerged wall jet above the gate lip (Figure 7d). These tornado-like vortices are responsible for creating hydrodynamic effects on the gate. As seen in Figure 7c, the separated flow from the sidewalls induced vortex structures in the flow direction, which stretched downstream in the roller region and dissipated in a relatively short distance due to prominent shear effects in this region. Such vortex structures may induce significant scour effects on the banks of an earth channel and oscillations on the gate.



**Figure 7.** Visualization of time-averaged three-dimensional flow structure using streamlines colored with pressure in (a) and vorticity magnitude in the remaining images: (a) side view; (b) top view; (c) front view; (d) three-dimensional view.



**Figure 8.** Time-averaged velocity vectors and recirculation zones on the free surface.

#### 4.3. Development of anti-Vortex Elements

Considering vortex structures revealed by the LES in the numerical analysis part of the study, four types of vortex breakers were designed and mounted on the downstream face of the gate as shown in Figure 9. Baffles were designed as either solid or porous to damp energy of existing vortices and reduce adverse hydrodynamic effects acting on the gate. Vertical baffles were located at the centers of counter-rotating vortex pair, where three-dimensional effects were found to be prominent experimentally (Figure 3b) and numerically (Figure 8). Horizontal baffles in Figure 9b,c were located at an elevation below the water surface level just downstream of the gate.

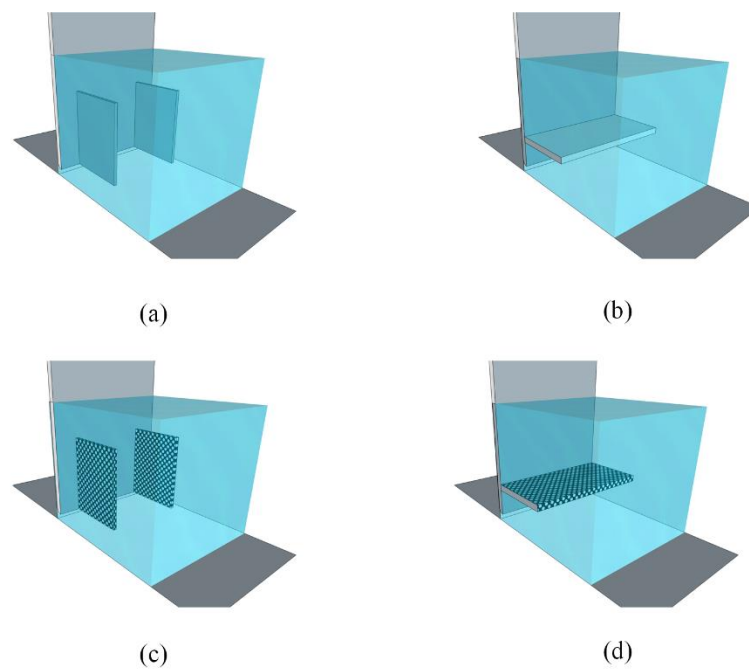


**Figure 9.** Vortex breakers mounted on the downstream face of the gate: (a) vertical solid baffle; (b) horizontal solid baffle; (c) vertical porous baffle; (d) horizontal porous baffle. The control volume is depicted as transparent volume.

In order to assess the vortex damping performance of each vortex breaker, a rectangular control volume was created at the downstream of the gate covering entire roller region. The volumetric averaged value of the magnitude of the mean vorticity ( $\bar{\omega} = \vec{\nabla} \times \vec{V}$ ) that was calculated based on the mean velocity field was calculated using the following definition:

$$|\bar{\omega}|_{av} = \frac{\int_{CV} |\bar{\omega}|}{V}, \quad (6)$$

where  $|\bar{\omega}| = \sqrt{\bar{\omega}_x^2 + \bar{\omega}_y^2 + \bar{\omega}_z^2}$  is the magnitude of the mean vorticity at a computational cell,  $V$  is the total volume of the control volume, and  $|\bar{\omega}|_{av}$  is the average value of the mean vorticity in the control volume, which is calculated as a scalar. Weighted average is performed with respect to the volume fraction value at a cell in order to exclude the empty cell while calculating the volume-averaged vorticity in Equation (6).

Turbulent flow through the porous baffle is simulated using Darcy–Forchheimer relation, which is valid for non-Darcy flows through porous media at high Reynolds numbers. The following source term is added to the right-hand side of momentum equations to represent drag effects encountered in the porous zone:

$$S_i = -\left(\vartheta D + \frac{1}{2} |\bar{U}_{ij}| F\right) \bar{u}_i, \quad (7)$$

where  $D$  and  $F$  are Darcy and Forchheimer coefficients, which can be calculated from the following empirical relations for a given porosity  $\varepsilon$  and median diameter  $d_{50}$ :

$$D = \frac{150(1-\varepsilon)^2}{d_{50}^2 \varepsilon^3}, \quad (8)$$

$$F = \frac{1.75(1-\varepsilon)}{d_{50} \varepsilon^3}. \quad (9)$$

Here, median diameter was determined from sand mixtures given in Sperry and Pierce [24] and Morgan [25] to specify corresponding porosities for different soil mixtures. Three different porosities were selected to observe the sensitivity of the performance of the vortex breaker to the porosity, and corresponding Darcy and Forchheimer coefficients are given in Table 3.

**Table 3.** Darcy and Forchheimer coefficients for different porosities.

Porosity ( $\epsilon$ )	$D(m^{-2})$	$F(m^{-1})$
0.31	$2.76 \times 10^9$	$5.24 \times 10^4$
0.504	$7.1 \times 10^7$	$4.78 \times 10^3$
0.802	$6.26 \times 10^5$	$3.54 \times 10^2$

The numerical model for the simulation of turbulent flow through a porous baffle was validated in the previous studies by comparing numerical results with the velocity measurements conducted in a mixing tank [22,26]. Numerical simulations were performed for the vortex breakers, as shown in Figure 9, using the same flow conditions as in the validation part. Volume-averaged values of the magnitudes of the mean vorticity were calculated for each case based on the numerical simulation results, and they are compared in Table 4 along with the damping ratios in comparison to the conventional design without baffle. Results show that the horizontal porous baffle with 0.3 porosity yielded the best damping performance among other designs considered in this study. The length of the horizontal baffle was set to 18 cm in these simulations.

**Table 4.** Comparison of vortex damping performance of each design in Figure 9. N/A—not applicable.

Design	Porosity ( $\epsilon$ )	$ \bar{\omega} _{av}$	Dissipation Ratio
No baffle	N/A	39.066	-
Vertical solid	N/A	34.417	11.90%
Horizontal solid	N/A	36.898	13.25%
Vertical porous	0.3	36.898	5.55%
Vertical porous	0.5	36.905	5.53%
Vertical porous	0.8	34.816	10.88%
Horizontal porous	0.3	32.504	16.80%
Horizontal porous	0.5	34.417	11.90
Horizontal porous	0.8	36.210	7.31

In order to evaluate the sensitivity of the damping performance of the horizontal porous baffle to the length, numerical simulations were repeated for different baffle lengths shown in Table 5 and  $\epsilon = 0.3$ . The length of baffle was non-dimensionalized with respect to the length of the roller that was predicted from Equation (4). Results in Table 5 show that the vortex breaking performance of the horizontal porous baffle is highly sensitive to the length of the baffle and dissipation performance can be improved as the length of the baffle increases.

**Table 5.** Comparison of vortex damping performance of horizontal porous baffle for different lengths. Here,  $L_{rsj}$  is calculated from Equation (4).

$L_{vb}/L_{rsj}$	$ \bar{\omega} _{av}$	Dissipation Ratio
0.10	34.423	16.80%
0.15	32.504	11.89%
0.31	28.594	26.80%

Vortex structures downstream of the gate are visualized using the  $Q$ -criteria ( $Q = -0.5\partial\bar{u}_i/\partial x_j\partial\bar{u}_j/\partial x_i$ ), which is calculated based on the mean velocity, and compared with the conventional gate design in Figure 10. As seen in Figure 10a, different vortex systems were captured

such as helical and horseshoe vortices, which play a critical role in the onset of hydrodynamic forces on the gate. Figure 10b demonstrates that the proposed anti-vortex element mounted on the downstream of the gate can successfully suppress these vortex structures.

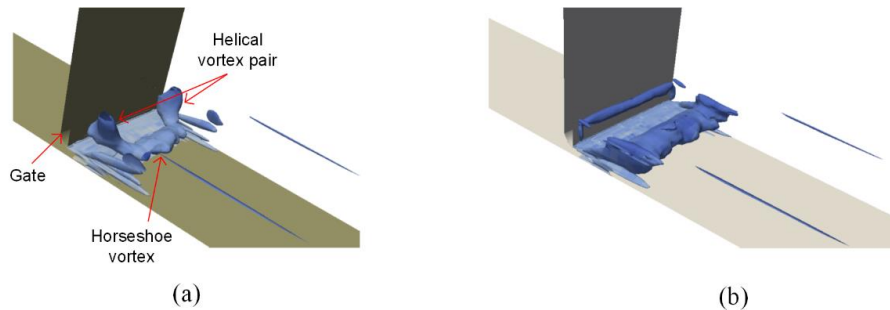


**Figure 10.** Visualization of vortex structures downstream of the submerged gate flow using the  $Q$ -criteria: (a) no baffle; (b) with horizontal porous baffle for  $\epsilon = 0.3$  and  $L/L_{rsj} = 0.31$ .

In order to further assess the performance of the proposed vortex breaker, time variation of lift forces on the gate lip and drag forces on the downstream face are compared in Figure 11 for a conventional gate design and the proposed breaker design. It should be noted that hydrodynamic pressures are considered while calculating forces acting on the gate. The proposed design could reduce time-averaged hydrodynamic forces acting on the gate lip by 9.4% and on the downstream face of the gate by 8.6%. The significant reduction in lift forces is associated with the suppression of unsteady vortex systems at the downstream, since recirculating flows in the roller region interact with the mean flow below the gate lip, which may contribute to the lift effects acting on the gate lip. The proposed horizontal porous baffle design successfully reduces vortex-induced hydrodynamic effects acting on the gate.

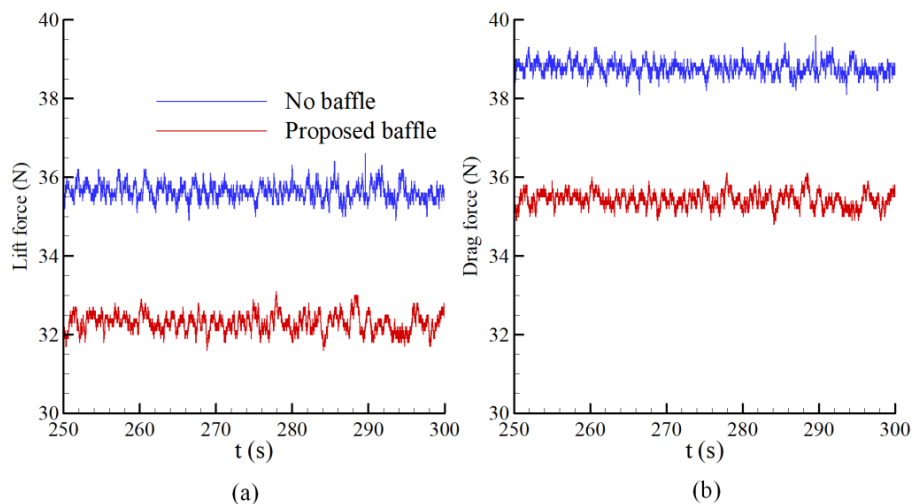


**Figure 11.** Time variations of (a) lift forces acting on the gate lip and (b) drag forces acting on the downstream face of the gate.

#### 4.4. Performance of the Vortex Breaker for Different Flow Conditions

The vortex breaker was tested for various flow conditions to assess vortex breaking performance under different flow conditions of inlet Froude number  $F_1$  and submergence ratio  $S$ . Different flow conditions are addressed in Table 6 to achieve this goal. Case 1 was the validation case used in the experimental and numerical studies in this study. Case 2 and Case 3 were produced for different Froude numbers keeping the submergence ratio as constant in order to evaluate the effect of the inlet

Froude number. In order to see the effect of the submergence ratio, which is another key parameter for the SHJ flow, Case 4 and Case 5 were produced to have different submergence factors for identical Froude numbers. The results show that the proposed design can mitigate vortex effects downstream of the submerged gate for different flow conditions.

**Table 6.** Vortex breaker for different flow conditions.

Case	Q (lt/s)	$y_1$ (mm)	$U_1$ (m/s)	$F_1$	Re	S	$ \bar{\omega} _{av}$		Vortex Dissipation Ratio (%)
							No Baffle	Breaker	
Case 1	21	25	2.1	4.24	$9.9 \times 10^4$	0.67	39.066	28.594	26.81
Case 2	15	25	1.5	3.03	$7.1 \times 10^4$	0.67	34.838	25.880	25.71
Case 3	25	25	2.5	5.05	$1.2 \times 10^5$	0.67	37.764	27.947	26.00
Case 4	21	25	2.1	4.24	$9.9 \times 10^4$	0.96	30.402	23.782	21.78
Case 5	21	25	2.1	4.24	$9.9 \times 10^4$	0.50	42.627	29.787	30.12

## 5. Conclusions

The experimental and numerical study summarized in this paper focused on an investigation of three-dimensional flow features in the SHJ that forms downstream of a vertical gate. Numerical simulation results were found to be consistent with the experimental measurements at different spanwise and streamwise locations downstream of the gate, where observed three-dimensional effects were significant. Simulation of the upstream flow in the current study provided vortex flow field at the inlet of the roller, which is more realistic than imposing a uniform velocity distribution below the gate. Helical vortex pairs and horseshoe vortex systems were captured in the roller using high-resolution numerical simulation results. Considering features of the identified vortex structures, different types of vortex breakers were developed on the downstream face of the gate and tested based on the numerical simulation results. Performance of each vortex breaker was numerically evaluated relying on the volume-averaged value of the magnitude of the mean vorticity in the roller. Numerical simulation results showed that the horizontal porous baffle mounted downstream of the gate can reduce vortices by 26.8% in the roller, as well as the lift and drag forces acting on the gate lip and downstream face of the gate by 9.4% and 8.6%, respectively. Numerical simulations conducted for different inlet Froude numbers and submergence factors revealed that the vortex breaker can reduce vortex effects by 21.78% to 30.12%. The anti-vortex element proposed in the present study may be implemented on existing sluice gates in irrigation canals and natural streams to reduce possible adverse hydrodynamic effects acting on the gate depending on the downstream flow conditions.

**Supplementary Materials:** The following are available at <http://www.mdpi.com/2073-4441/12/3/750/s1>.

**Author Contributions:** Conceptualization, E.D. and M.M.A.; methodology, E.D.; software, E.D.; validation, E.D. and M.M.A.; formal analysis, E.D. and M.M.A.; investigation, E.D. and M.M.A.; writing—original draft preparation, E.D. and M.M.A.; writing—review and editing, M.M.A.; visualization, E.D.; supervision, M.M.A.; project administration, E.D.; funding acquisition, E.D. All authors read and agreed to the published version of the manuscript.

**Funding:** This work was supported by the Scientific and Technological Research Council of Turkey (TUBITAK) under Grant no. 216M521, and by the Scientific Research Project of Eskisehir Osmangazi University (Project No. 201715007).

**Acknowledgments:** The numerical calculations reported in this paper were fully performed at TUBITAK ULAKBIM, High-Performance and Grid Computing Center (TRUBA resources).

**Conflicts of Interest:** The authors declare no conflicts of interest.

## References

1. Long, D.; Steffler, P.M.; Rajaratnam, N. LDA study of flow structure in submerged hydraulic jump. *J. Hydraul. Res.* **1990**, *28*, 437–460. [[CrossRef](#)]
2. Demirel, E. Measured and simulated flow downstream of the submerged sluice gate. *Water Environ. J.* **2015**, *29*, 446–455. [[CrossRef](#)]

3. Liu, M.; Rajaratnam, N.; Zhu, D.Z. Turbulence Structure of Hydraulic Jumps of Low Froude Numbers. *J. Hydraul. Eng.* **2004**, *130*, 511–520. [[CrossRef](#)]
4. De Dios, M.; Bombardelli, F.A.; García, C.M.; Liscia, S.O.; Lopardo, R.A.; Parravicini, J.A. Experimental characterization of three-dimensional flow vortical structures in submerged hydraulic jumps. *HydroResearch* **2017**, *15*, 1–12. [[CrossRef](#)]
5. Dey, S.; Sarkar, A. Response of velocity and turbulence in submerged wall jets to abrupt changes from smooth to rough beds and its application to scour downstream of an apron. *J. Fluid Mech.* **2006**, *556*, 387. [[CrossRef](#)]
6. Dey, S.; Sarkar, A. Characteristics of Turbulent Flow in Submerged Jumps on Rough Beds. *J. Eng. Mech.* **2008**, *134*, 49–59. [[CrossRef](#)]
7. Bhargava, V.P.; Narasimhan, S. Pressure fluctuations on gates. *J. Hydraul. Res.* **1989**, *27*, 215–231. [[CrossRef](#)]
8. Thang, N.D.; Naudascher, E. Vortex-excited vibrations of underflow gates. *J. Hydraul. Res.* **1986**, *24*, 133–151. [[CrossRef](#)]
9. Billeter, P.; Staubli, T. Flow-induced multiple-mode vibrations of gates with submerged discharge. *J. Fluids Struct.* **2000**, *14*, 323–338. [[CrossRef](#)]
10. Erdbrink, C.; Krzhizhanovskaya, V.V.; Sloot, P. Reducing cross-flow vibrations of underflow gates: Experiments and numerical studies. *J. Fluids Struct.* **2014**, *50*, 25–48. [[CrossRef](#)]
11. Long, D.; Steffler, P.M.; Rajaratnam, N. A numerical study of submerged hydraulic jumps. *J. Hydraul. Res.* **1991**, *29*, 293–308. [[CrossRef](#)]
12. Ma, F.; Hou, Y.; Prinos, P. Numerical calculation of submerged hydraulic jumps Calcul numérique des sauts hydrauliques submergés. *J. Hydraul. Res.* **2001**, *39*, 493–503. [[CrossRef](#)]
13. Javan, M.; Eghbalzadeh, A. 2D numerical simulation of submerged hydraulic jumps. *Appl. Math. Model.* **2013**, *37*, 6661–6669. [[CrossRef](#)]
14. Cassan, L.; Belaud, G. Experimental and Numerical Investigation of Flow under Sluice Gates. *J. Hydraul. Eng.* **2012**, *138*, 367–373. [[CrossRef](#)]
15. Jesudhas, V.; Roussinova, V.; Balachandar, R.; Barron, R. Submerged Hydraulic Jump Study Using DES. *J. Hydraul. Eng.* **2017**, *143*, 04016091. [[CrossRef](#)]
16. Nortek, A. *Vectrino Velocimeter User Guide*; Tech. Rep.; Nortek AS: Vangkroken, Norway, 2019.
17. Wahl, T.L. Analyzing ADV data using WinADV. In Proceedings of the Joint Conference on Water Resources Engineering and Water Resources Planning & Management, ASCE, Reston, VA, USA, 31 July–2 August 2000; pp. 1–10.
18. Yeh, H.H. Vorticity-generation mechanisms in bores. *Proc. R. Soc. Lond. Ser. A Math. Phys. Sci.* **1991**, *432*, 215–231.
19. OpenFOAM. *The OpenFOAM Foundation*; OpenCFD Ltd. Bracknell: London, UK, 2015.
20. Hirt, C.; Nichols, B. Volume of fluid (VOF) method for the dynamics of free boundaries. *J. Comput. Phys.* **1981**, *39*, 201–225. [[CrossRef](#)]
21. Wu, S.; Rajaratnam, N. Free jumps, submerged jumps and wall jets. *J. Hydraul. Res.* **1995**, *33*, 197–212. [[CrossRef](#)]
22. Kizilaslan, M.A.; Demirel, E.; Aral, M.M. Efficiency Enhancement of Chlorine Contact Tanks in Water Treatment Plants: A Full-Scale Application. *Processes* **2019**, *7*, 551. [[CrossRef](#)]
23. Roth, A.; Hager, W.H. Underflow of standard sluice gate. *Exp. Fluids* **1999**, *27*, 339–350. [[CrossRef](#)]
24. Sperry, J.M.; Peirce, J.J. A Model for Estimating the Hydraulic Conductivity of Granular Material Based on Grain Shape, Grain Size, and Porosity. *Ground Water* **1995**, *33*, 892–898. [[CrossRef](#)]
25. Morgan, N.A. PHYSICAL PROPERTIES OF MARINE SEDIMENTS AS RELATED TO SEISMIC VELOCITIES. *Geophysics* **1969**, *34*, 529–545. [[CrossRef](#)]
26. Kizilaslan, M.A.; Demirel, E.; Aral, M.M. Effect of Porous Baffles on the Energy Performance of Contact Tanks in Water Treatment. *Water* **2018**, *10*, 1084. [[CrossRef](#)]

